Acceleration of Particle-In-Cell Simulations using Sparse Grid Algorithms

L. Garrigues, M. Chung-To-Sang, G. Fubiani, C. Guillet, F. Deluzet, J. Narski

Acceleration of Particle-In-Cell Simulations using Sparse Grid Algorithms. II. Application to Partially Magnetized Low Temperature Plasmas

L. Garrigues,[1] M. Chung-To-Sang,[1] G. Fubiani,[1] C. Guillet,[1,2] F. Deluzet,[2] and J. Narski[2]
[1)] *LAPLACE, Université de Toulouse, CNRS, INPT, UPS, Toulouse, France*
[2)] *Université de Toulouse, UPS, INSA, UT1, UTM, Institut de Mathématiques de Toulouse, CNRS, Institut de Mathématiques de Toulouse, UMR 5219, 31062 Toulouse, France*

(*Electronic mail: laurent.garrigues@laplace.univ-tlse.fr)

(Dated: 16 July 2024)

In the companion paper[L. Garrigues *et al.*, submitted to Physics of Plasmas], we have extended the sparse PIC approach already used in the literature with the offset scheme to reduce the grid-based error. In this study, we demonstrate the ability of the offset sparse PIC algorithm to model partially magnetized low-temperature plasmas by reducing the grid-based error. In the context of multi-cusp magnetic field configurations, the offset scheme reduces the error of the current collected at the walls to less than 5% for more of the plasma conditions encountered in ion source applications. The formation of a double layer in the sheath region is also captured. In the context of the electron drift instability that occurs in the Hall thruster, the plasma properties as well as the ion velocity distribution function can be retrieved with a high enough precision without considering an initial regular grid with a smaller mesh resolution. The results also highlight the advantage of combining the electric potential at the nodes of the regular grid instead of directly combining the electric field from the component grids. Compared to the regular PIC algorithm, the typical speed-up factor is about 3 for a number of mesh nodes of 256^2 and 5 for 512^2.

I. INTRODUCTION

The enhancement of plasma confinement using multi-cusp magnetic field topology was proposed in the early 1970s[1] thanks to the special arrangement of magnetic rods proposed by Sadowski[2] and Yoshikawa *et al.*[3], originally thought to produce high-energy particles and high current densities for fusion devices. Later, the multi-cusp magnetic field coupled with low pressure discharges was used to produce positive and negative ion beams for ion source applications[4]. In parallel, many fundamental studies have been performed to propose scaling laws for charged particle losses for various plasma parameters such as magnetic field strength, pressure, ion mass, etc. (see Ref.[5] and references therein). In the literature, this type of discharge, which includes magnetized electrons and unmagnetized ions, falls into the category of partially magnetized low-temperature plasmas. A 2D particle-in-cell Monte Carlo collision PIC-MCC model has recently been used to address the question of particle losses in this context[5]. The complex topology of the magnetic field raises the question of the ability of the sparse PIC approach to recover the solution obtained with the regular PIC model. The main issue is the capture (or not) of the electron transport, which is impeded in the direction perpendicular to the magnetic field, while it is almost free along the magnetic field, and the grid-based error associated with the combination technique associated with the sparse PIC schemes.

Another example of a partially magnetized low-temperature plasma is the Hall thruster used for satellite propulsion.[6–8]. In a Hall thruster, an E×B direction instability occurs in the mm wavelength and MHz frequency range due to the difference in charged particle transport, with magnetized and drifting electrons and unmagnetized ions being axially accelerated. The electron cyclotron drift instability (EDI) resulting from the coupling between electron Bernstein modes and ion acoustic waves was studied by Gary in the early 1970s (see Ref.9) by resolving the dispersion relation in the linear phase of the instability. This work has been revisited and applied to the typical conditions of a Hall thruster to determine the conditions for the existence of unstable modes and the associated growth rates[10–13]. Comparisons with existing coherent Thomson scattering measurements have been made[14–16]. 2D PIC simulations including the azimuthal - E×B - and axial - E - planes have been performed to go beyond the linear regime solution and to determine the unstable mode characteristics and the origin of the saturation mechanism[17,18]. The typical conditions of this later work served as a reference for a benchmark to evaluate the influence of numerical issues (PIC cycle implementation, programming languages, parallelization method and its implementation, processor architectures, etc.) on the results of seven independent PIC codes[19]. The basis of this 2D PIC benchmark was later also used for complementary work to understand the coupling between the EDI and the ion-ion two-stream instability when multiply charged ions are considered[20,21]. The space and time variations of plasma properties obtained with the regular PIC approach in the context of the EDI have already served to challenge the sparse PIC algorithm in recent years[22]. A large grid-based error is introduced when the hierarchy of component grids is constructed from the same regular grid resolution as the standard PIC approach for comparisons. One way to reduce the grid-based error, but at the cost of reducing the speed-up factor, is to construct a hierarchy of component grids from a regular grid with a higher resolution.

The objectives of this study are focused on the use of the sparse PIC algorithms (including the offset method) as well as the effect of the combination technique (in nodal or hierarchical basis) on the multi-cusp magnetic field configuration (section II) and the Hall thruster (section III). Throughout the text, the notations for the sparse PIC methods are the same as in the companion paper[23]. In section IV we evaluate the ability of the sparse PIC algorithms to model other partially

magnetized low-temperature plasmas. We end with a conclusion (section V).

II. MULTI-CUSP MAGNETIC FIELD CONFIGURATIONS

In section II A we describe the plasma source model including the simulation domain and the plasma generation. Simulation results are presented in section II B. A discussion focusing on the potential of sparse PIC approaches to model cusp magnetic field discharges is also included.

A. Plasma source model description

1. Simulation domain and magnetic field profile

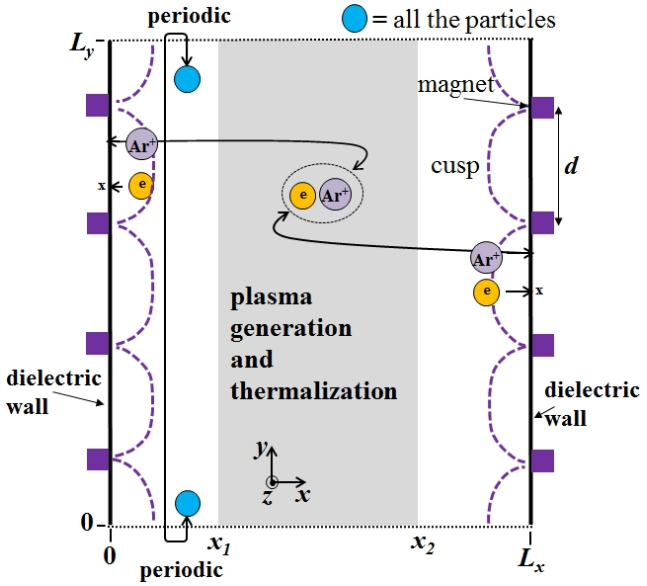

FIG. 1. Computational domain.

The 2D PIC simulation domain is square with a length of $L_x = L_y = 40$ mm (see Fig.1). It contains four magnets with a distance d equal to 10 mm along the y direction, periodic boundary conditions are used to simulate an infinite sequence of magnetic rods. The magnets are alternately oriented south-north and north-south to achieve a cusp field profile. The magnets are 40 mm apart along the x direction. The left and right walls are dielectrics with an equal flow of ions and electrons in the steady state regime.

The magnetic field profile is taken from the work of Lieberman and Lichtenberg[24]. Assuming that the width of the magnet is smaller than the distance between the magnets, the magnetic field components along the x and y directions, denoted B_x and B_y respectively, are given by

$$\begin{aligned} & x < x_m \\ B_x(x,y) &= B_0 \sin(\pi y/d) e^{-\pi x/d} \\ B_y(x,y) &= -B_0 \cos(\pi y/d) e^{-\pi x/d} \\ & x \geq x_m \\ B_x(x,y) &= -B_0 \sin(\pi y/d) e^{-\pi (L_x - x)/d} \\ B_y(x,y) &= -B_0 \cos(\pi y/d) e^{-\pi (L_x - x)/d} \end{aligned} \quad (1)$$

where x_m is the mid-plane along x and B_0 is the maximum magnetic field strength. Note that the width of the magnet only affects the maximum magnetic field, which is included in our definition in B_0. We also assume that the self-induced magnetic field is negligible, since the current driven by the charged particles of the plasma remains very small.

The magnetic field strength, defined as $B(x,y) = \sqrt{B_x(x,y)^2 + B_y(x,y)^2}$ around a magnet, is shown in Fig.2. The magnetic field strength decreases exponentially from the magnet to the center of the plasma discharge along the x direction with a length equal to d/π, but it does not depend on y. The magnetic field lines are also shown in Fig.2. The magnetic field lines are almost perpendicular to the walls at the location of the magnet (cusp field region), while they become divergent when moving along the y direction. In all of these studies, the magnetic field strength is small enough to trap only the electrons. The electrons that wrap around the magnetic field lines are reflected by the strong magnetic field at the location of the magnet (mirror effect) or lost at the wall surface, depending on the ratio of the parallel to the perpendicular velocity component (loss cone angle[25]). The maximum of the magnetic field strength B_0 is considered as a variable parameter.

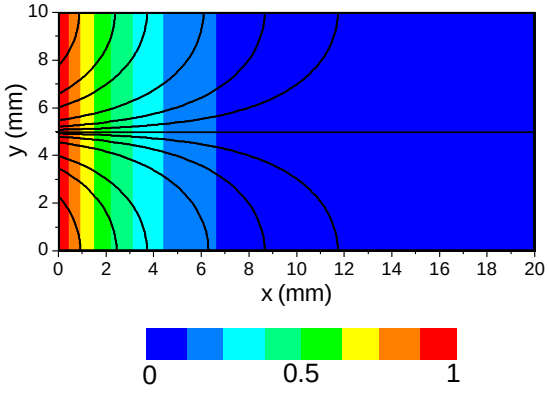

FIG. 2. Magnetic field strength normalized by the maximum B_0 (color scale) and magnetic field lines (black lines) close to a magnet.

TABLE I. Physical and initial numerical parameters for the cusp field benchmark.

Simulation domain	
wall distance along x, L_x (mm)	40
plane distance along y, L_y (mm)	40
left injection plane position, x_1 (mm)	16
right injection plane position, x_2 (mm)	24
Physical parameters	
electron mass m_e (10^{-31} kg)	9.11
ion mass m_i (10^{-26} kg)	6.683
Initial conditions	
plasma density n_0 (10^{15} m^{-3})	1
electron temperature T_e (eV)	2
thermalization temperature T_h (eV)	2
thermalization frequency ν_h (s^{-1})	1.5×10^9
ion temperature T_i (eV)	0.2
neutral density N	variable
neutral temperature T_N (K)	300
magnet distance d (mm)	10
magnetic field strength B_0	variable
Initial parameters	
regular PIC, grid cell number	256^2
regular PIC, grid spacing $\Delta x = \Delta y$	$L_x/256 = L_y/256$
time step Δt	$0.2/\omega_p$
initial number of particles per cell N_{pc}	50
Boundary conditions	
left wall	dielectric
right wall	dielectric
top wall	periodic
bottom wall	periodic

2. Plasma generation and collisions

Unlike the previous benchmark comparison in the context of dual-frequency capacitive discharges, where the plasma is self-consistently maintained by the ionization events[23], the plasma generation in this study is treated in a different manner. First, a plasma density with an equal number of ions and electrons is injected. To simulate the ionization processes, each time an ion is lost on the dielectrics, an electron-ion pair with a Maxwellian initial distribution (but with different initial temperature) is randomly injected into a given region in the center of the plasma discharge (slab region between x_1 and x_2 along the x direction). Electrons escaping from the dielectric walls are eliminated and not replaced in the simulation. This keeps the total number of ions in the simulation constant and a fixed averaged plasma density equal to the initial one. This also speeds up the time to reach the steady state solution and has been used successfully in previous studies[5,23,26–28]. This last advantage of decoupling the plasma generation from the neutral pressure (or density for a fixed neutral temperature, as in this study) is to perform parametric studies for different neutral pressures while keeping the plasma density the same.

Because high-energy electrons are lost at the walls, the tail of the distribution is depleted and the electron temperature is lower than the imposed electron temperature in the plasma bulk. To maintain a constant electron temperature and a Maxwellian distribution of electrons in the plasma bulk, a thermalization process is used[5,23,27–29]. It consists in isotropically refreshing the velocity components of the electrons with a Maxwellian distribution at a temperature $T_h = T_e$ in a given region at a constant frequency ν_h. Obviously, this "additional" collision process releases the electrons. As long as this process takes place far away from the cusp field region, in the region of low magnetic field, this "fictitious" induced transport does not modify the electron transport in the zone of interest (magnet region). The thermalization region is the same as the bulk plasma injection region. The thermalized frequency is set to 1.5×10^9 s^{-1}. For electrons with a Maxwellian distribution at a temperature of 2 eV, the electrons are thermalized on average ~ 6 times. Charged particles crossing the top or bottom planes are re-emitted at the opposite plane at the same axial position with the same velocity components.

The gas is argon. In the electron neutral collision cross sections we have considered only the momentum process, which is the dominant process for electron neutral scattering. The cross section data are taken from the database of A. V. Phelps[30]. As already mentioned, the neutral density is considered as a parameter. For the typical range of ion energies, the main process of ion-neutral collisions is backscattering (charge exchange). For a cross section in the range of 3 to 4 $\times 10^{-19}$ m^{-2} (Ref. 31), and for a pressure varying from 0.01 to a few mTorr, the ion-neutral mean free path is larger than the simulation domain. Since the ions are not magnetized, the contribution of the ion-neutral collisions is negligible (this has been confirmed in the work of Jiang *et al.*[5]).

All input parameters of the simulations are listed in the table I. The implementation of the periodic boundary conditions is the same as in the companion paper (see Ref.23 for more details). The approximate method that models the charging walls (dielectric) with a capacitance is given in Jiang *et al.*[5].

To meet the stability criteria, in the regular PIC model the number of grid cells is set to resolve the electron Debye length, while the time step used for both electrons and ions is a fraction of the reciprocal of the electron plasma frequency. No subcycling is performed. Typically, 256^2 grid cells are used for the regular PIC approach. For the sparse algorithms we performed the calculations with a regular grid $2^I \times 2^J$ with $I = J = n = 8$ and with l^0 varying from 0 (standard sparse approach) to 4 (offset sparse algorithms), keeping $l^1 = 1$ (see Ref.23 for notations). The two methods for calculating the electric field at the particle location (using the hierarchical or nodal approaches, labeled HSg and NSg, respectively) were also tested.

B. Simulation results and discussion

Comparisons between the regular and sparse PIC methods have been performed for the conditions of Table I. All calculations were performed on the Laplace supercomputer, 2 × Skylake per node (Intel Xeon Gold 6226R, 2.90 GHz, 16 cores), using Intel compiler version 2021.2.0 and IntelMPI version 2021.2. A typical ion density profile is shown in Fig.3 for the regular PIC approach (denoted by the notation PIC - Fig. 3a) and the sparse approach for the nodal basis approach, with the notation PIC-NSg (with $l^0 = 0$ and $l^1 = 0$, standard method) and PIC-ONSg (with $l^0 = 4$ and $l^1 = 1$, offset approach), in Fig. 3b and Fig. 3c, respectively. The pressure is fixed at 0.1 mTorr and the maximum magnetic field strength is $B_0 = 400$ G. The magnets are located at $y = 5$, 15, 25 and 35 mm.The profile shown is representative of the ion density variations we can expect in a cusp field discharge. The maximum density is localized in the injection and thermalization region in the center of the simulation domain with an almost constant density profile. In front of the magnets, the density decreases as the ions are accelerated in the pre-sheath at the end of the injection region. A sheath is formed in front of the magnet as in unmagnetized plasmas. In the region between the cusps, in order to maintain quasineutrality, the ion density profile is almost parallel to the walls as the magnetic field lines, since the electron motion in the direction perpendicular to the magnetic field is impeded. A sharp gradient of ion density takes place in this region, as we see in Fig.3, induced by the reduced electron transport through the magnetic field. The current loss is mainly concentrated in the region of charged particle losses (in the cusp region), while it is negligible between the cusps. We note that while the standard sparse PIC approach (see Fig.3b) is able to qualitatively capture the ion density profile, especially the region of maximum plasma density established and controlled by injection and thermalization processes, there are differences outside this region. The method reproduces the shape of the ion density in the region of high magnetic field strength, but with a certain error that leads to a smoothing of the density gradient along both x and y directions. This is a clear signature of the grid-based error associated with the combination technique when the dominant terms in the error are along the mixed directions (see Refs. 23, 32–34). The advantage of the offset method[23,34], which consists in reducing the coarser resolution of the component grids and excluding the more anisotropic ones, is clearly visible in Fig.3c. The ion density profile is now captured more accurately. The main drawback of the offset method is the increase in the number of cells in the component grids as shown in our companion paper[23]. Accordingly, the total number of particles N_T increases to maintain the same number of particles per cell (same statistical error). Strictly speaking, N_T goes from 3.3×10^5 to 9.2×10^5 as l^0 goes from 0 to 4.

We show in Fig. 4 a one dimensional profile of the ion density along the y direction close to the left wall at $x = 3$ mm for the standard and sparse PIC methods, gradually increasing the l^0 parameters from 0 (standard sparse PIC, labeled PIC-NSg) to 4, keeping $l^1 = 1$ as in Fig. 3. It is interesting to note that the effect of the grid-based error is to smooth the ion

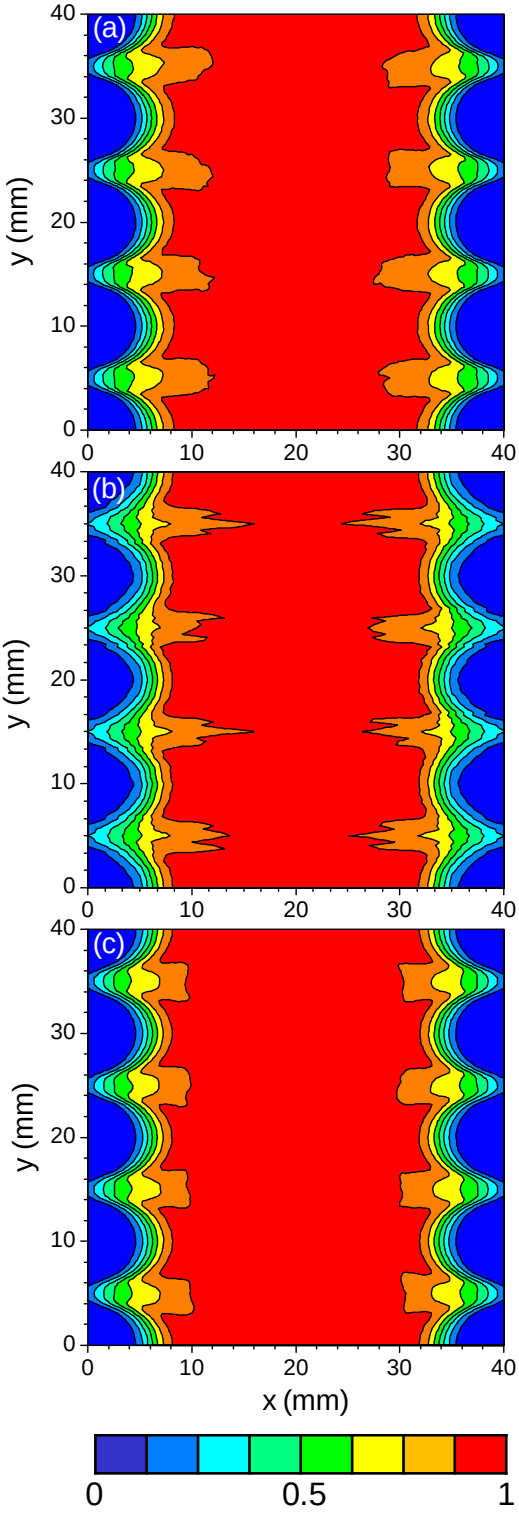

FIG. 3. Two dimensional ion density profile for different PIC algorithms, (a) standard PIC (maximum of 1.36×10^{15} m^{-3}, the total number of particles N_T is 3.3×10^6), (b) PIC-NSg with $l^0 = 0$ and $l^1 = 0$ (maximum of 1.43×10^{15} m^{-3}, $N_T = 3.3 \times 10^5$) and (c) PIC-ONSg with $l^0 = 4$ and $l^1 = 1$ (maximum of 1.36×10^{15} m^{-3}, $N_T = 9.2 \times 10^5$). The maximum magnetic field strength is $B_0 = 400$ G and the pressure is 0.1 mTorr.

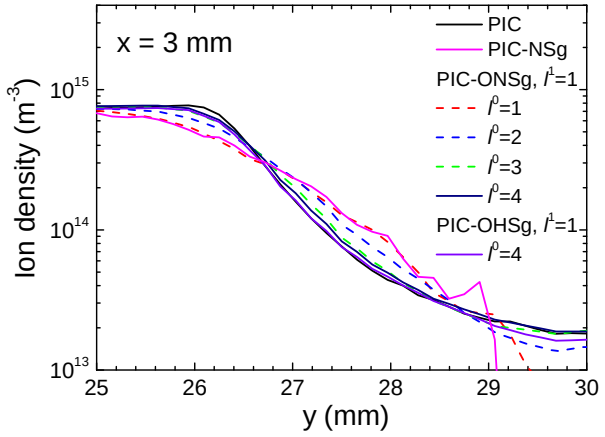

FIG. 4. One dimensional ion density profile along the y direction at a position x = 3 mm for different PIC algorithms (log scale). Calculations are performed with the standard and offset sparse methods with different l^0 parameters are shown keeping $l^1 = 1$. The results also illustrate the nodal and the hierarchical approaches. Same conditions than Fig.3.

density profile. As expected, as l^0 increases, the grid-based error decreases and the profile computed with the sparse approach becomes closer and closer to that of the standard PIC. For l^0, ≥ 3, the error for the 2D profiles of the electron and ion densities is less than 5 % (see table II). The calculations were carried out mainly with the nodal approach. We recall that it consists in using the nodal basis to recombine the electric potential on the regular Cartesian grid, then differentiating the electric field on the Cartesian grid and finally calculating the electric field at the particle location. In the hierarchical algorithm, the electric field at the particle location is calculated on each of the component grids and the combination technique is used to calculate the electric field at the particle location. Simulations of dual-frequency RF discharges have shown a reduced error when the nodal approach is used[23]. The comparison between the two approaches for the same parameters leads to the same conclusion when comparing the one dimensional ion density profiles of Fig.3 and the calculation error of Table II.

An interesting phenomenon has been highlighted in the work of Jiang *et al.*[5] for high magnetic field strength regimes with the appearance of a double sheath layer. We have tested the ability of the sparse PIC with the offset algorithm to capture this effect. For the same pressure as in Fig.3, in Fig.5 we show one-dimensional profiles in front of the magnet at y = 5 mm near the left wall for two magnetic field strengths B_0. In Fig.5a, at relatively low B_0, a classical unmagnetized sheath occurs close to the wall surface with an ion density greater than the electron density, while the situation changes when B_0 exceeds a certain limit (see Fig.5b). The reason is attributed to the mirror effect[35]. As the maximum of the magnetic field strength increases, it becomes more and more difficult for the electrons to reach the magnet and a negative sheath region (excess of negative charges) appears between the standard ion sheath and the plasma core[5]. It should be noted that this particular behavior is captured at high magnetic field strength

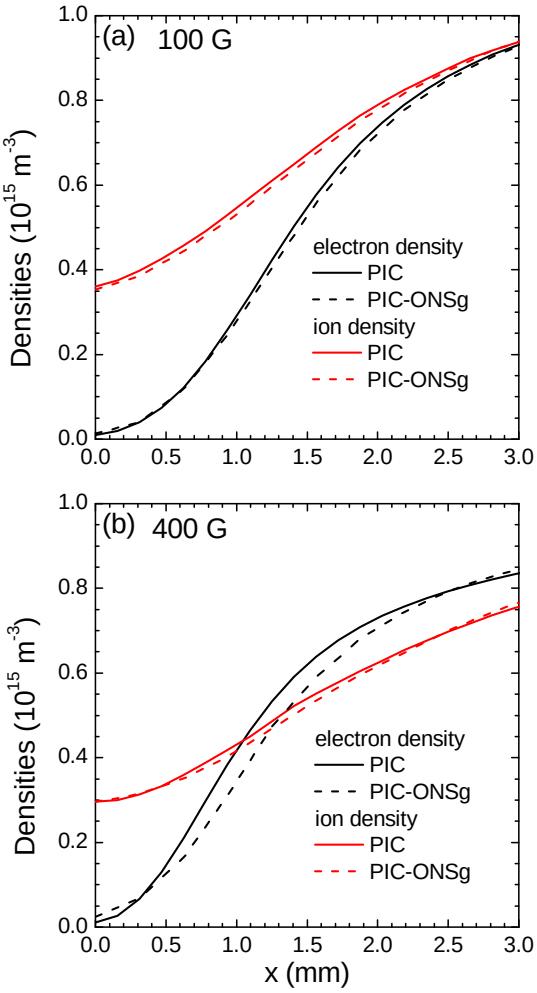

FIG. 5. One dimensional ion and electron densities profiles along the x direction at a position y = 5 mm for different PIC algorithms, (a) B_0 = 100 G, (b) B_0 = 400 G. Calculations with the sparse algorithm are made in the nodal basis with the offset method with $l^0 = 4$ and $l^1 = 1$. The pressure is 0.1 mTorr.

with the sparse PIC method.

We conclude this section by calculating the error (L2-norm[23,36]) on the current collected at the walls for a wide range of parameters, keeping $l^0 = 4$ and $l^1 = 1$ (see table II). The results are shown in Fig.6. A deficiency in the capture of the plasma properties associated with the grid-based error has consequences for the current collected at the wall surfaces. An estimate of the precision error in the calculation of this quantity is one way of determining the limit of the sparse method. The error remains (less than 5 %) independent of the pressure for $B_0 \leq 400$ G. For very low pressure and high magnetic field strength, the error becomes larger than 25 %. Increasing l^0 to a value higher than 4 would obviously reduce the error in the current and plasma properties, but with the drawback of reducing the computational gain due to the increase in the total number of particles to maintain the same statistical error. This is confirmed by the calculation of the execution acceleration time factor, which decreases from 5.6 to 3.1 (see the last line

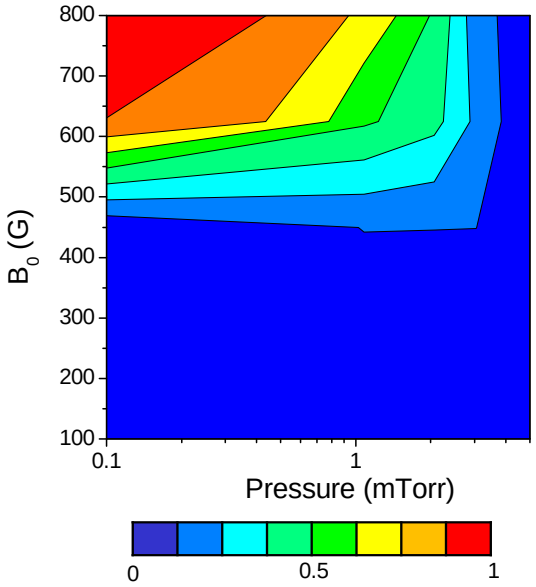

FIG. 6. Calculation in % of the error on the current collected at the walls (maximum 27 %) as a function of pressure and magnetic field strength. Calculations with the sparse algorithm are made in the nodal basis with the offset method with $l^0 = 4$ and $l^1 = 1$.

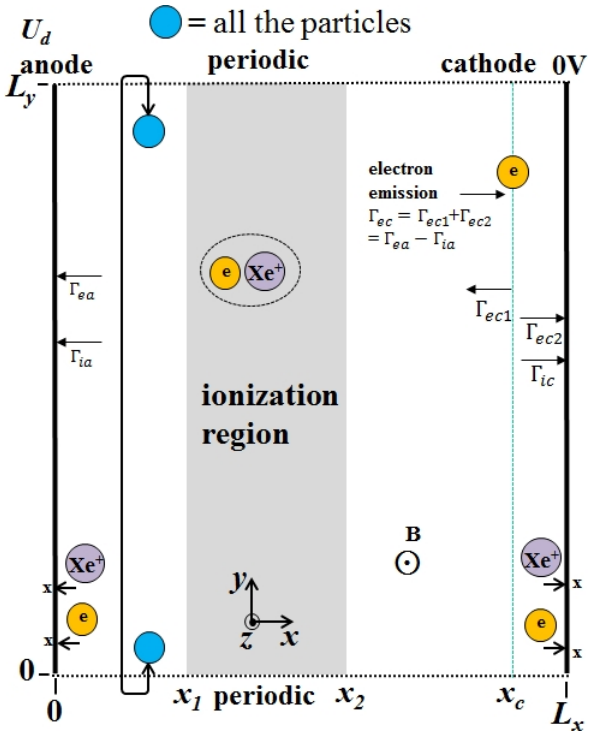

FIG. 7. Computational domain. The parameters x_1, x_2, and x_c refer to left and right injection planes and the axial position of the cathode. The charged particle fluxes averaged along the y direction Γ_{ea}, Γ_{ia}, Γ_{ec}, Γ_{ec1}, Γ_{ec2}, and Γ_{ic} stands for electron and ion fluxes at the anode, through the cathode, and through the exhaust planes, respectively.

TABLE II. Calculation of the error (%) on the profiles of the electron and ion densities and execution time acceleration factor. The conditions are the same than Fig.3.

PIC-ONSg, $l^0 =$	0	1	2	3	4	PIC-OHSg , $l^0 = 4$
n_i	7.2	6.9	5.3	4.9	4.6	5.0
n_e	7.6	7.1	5.4	4.9	4.6	5.0
speed up factor	5.6	7.9	6.1	4.9	3.1	2.7

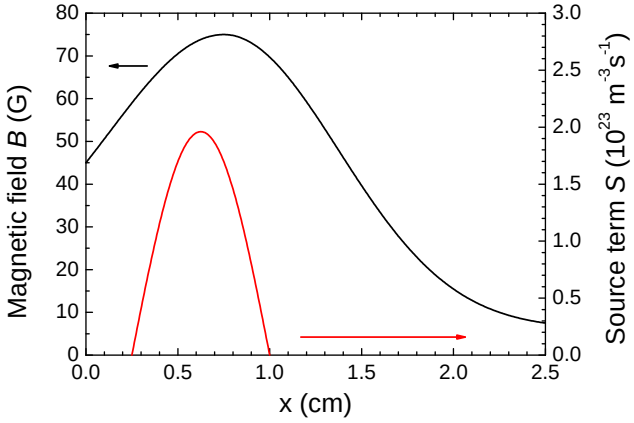

FIG. 8. Profiles of magnetic field strength B and ionization source term S.

of table II). The high acceleration factor $l^0 = 1$ is simply consistent with the decrease in the total number of particles for this very specific configuration (when $l^0 = l^1$). Interestingly, for $l^0 = 2$, the total number of particles has increased compared to $l^0 = 0$, and so has the acceleration factor. This is certainly due to the smaller number of component grids coupled with the specific arrangement of the number of cores taken in this study. We leave the optimization of the sparse PIC algorithms using the combined OpenMP and MPI parallelization techniques for future studies, but this highlights the degree of margin to reduce the speedup we still have for higher l^0 and l^1 factors. The use of the PIC-OHSg algorithms also reduces the speedup factor (as already mentioned in ref. 23).

III. HALL THRUSTER

A. Plasma model description and initial conditions

The simulation domain is in two dimensions (axial x and azimuthal y directions, whose lengths are denoted L_x and L_y, respectively) using Cartesian coordinates. The physical and initial numerical parameters for this study are given in table III. We start the simulation with a constant plasma density

TABLE III. Physical and initial numerical parameters for the Hall thruster benchmark.

Simulation domain	
axial length x, L_x (cm)	2.5
azimuthal length y, L_y (cm)	2.5
voltage, U_d (V)	200
current density, J_M (A/m^2)	150
left injection plane position, x_1 (cm)	0.25
right injection plane position, x_2 (cm)	1
axial position of the cathode, x_c (cm)	2.4
maximum magnetic field, B_M (G)	75
axial position of maximum magnetic field, x_B (cm)	0.75
Physical parameters	
electron mass m_e (10^{-31} kg)	9.11
ion mass m_i (10^{-25} kg)	2.1887
Initial conditions	
plasma density n_0 (10^{16} m^{-3})	8
electron temperature T_e (eV)	10
ion temperature T_i (eV)	0.5
Initial parameters	
regular PIC, grid cell number	512^2
regular PIC, grid spacing $\Delta x = \Delta y$	$L_x/512 = L_y/512$
time step Δt (s)	10^{-11}
initial number of particles per cell N_{pc}	400
Boundary conditions	
left wall	electrode, U_d
right wall	electrode, 0 V
top wall	periodic
bottom wall	periodic

with the same number of xenon ions and electrons, assuming Maxwellian distributions with different temperatures. At each time step, a certain number of charged particles is injected into a region called the ionization region (see the gray region in Fig.7 and the profile shown in Fig.8). A given amount of electrons (whose flux is noted Γ_{ec}) is injected into the cathode plane at a position noted x_c. The number of electrons to be injected is determined by the current conservation equation. The difference between the electron and ion flux at the anode, called Γ_{ea} and Γ_{ia} respectively, is calculated at each time step. If $\Gamma_{ea} > \Gamma_{ia}$, the difference $\Gamma_{ec} = \Gamma_{ea} - \Gamma_{ia}$ is injected at x_c, otherwise no electrons are injected. A fraction of Γ_{ec}, indicated as Γ_{ec1} in Fig.7, goes to the $x = 0$ plane, while the other fraction Γ_{ec2} neutralizes the ion beam crossing the $x = L_x$ plane Γ_{ic2}. Obviously, at steady state, $\Gamma_{ec2} = \Gamma_{ic2}$. The magnetic profile is perpendicular to the simulation domain and its profile is shown in Fig.8. The magnetic field strength makes the effect of the magnetic field on the ions negligible. To reduce the computational time, only a fraction of the azimuthal circumference (y direction) is modeled, periodic boundary conditions are used on the top and bottom planes, while Dirichlet boundary conditions are used on the left and right planes with a potential fixed at U_d and 0, respectively. Charged particles moving through the periodic planes are reinjected through the opposite plane, while those crossing the left and right planes are removed from the system. More information about the model description can be found elsewhere, in particular the analytical formula of the magnetic field and ionization source term profiles are given[17,19,22]. The electron Debye length λ_{de} for maximum plasma densities on the order of 2×10^{17} m^{-3} and an electron temperature of 50 eV is about 100 μm. The explicit PIC scheme requires 512^2 cells, while maintaining some latitude in the resolution of the grid spacing. Also, the resolution of the reciprocal of the electron plasma frequency imposes a time step Δt of 10^{-11} s. All simulations were performed on the Calmip Olympe supercomputer with 5 $\times$ Skylake nodes (Intel Xeon Gold 6140 bi-processors at 2.30 GHz with 18 cores each), using the Intel Compiler version 18.2.199 and IntelMPI version 18.2.

B. Simulation results and discussions

This section provides detailed comparisons between the regular PIC and sparse PIC approaches. For the sparse algorithms, we performed the computations on a regular $2^I \times 2^J$ grid with $I = J = n = 9$ and with $l^0 = 0$ (standard sparse approach) and $l^0 = 3$ (offset sparse algorithms), keeping $l^1 = 1$ (see Ref. 23 for notation). The two methods for calculating the electric field at the particle location (using the hierarchical or nodal approaches, labeled HSg and NSg, respectively) were also tested. The initial number of particles N_{pc} is fixed to 400 and the total number of particles (for one species) is $N_T = 1 \times 10^8$. Applying the formula for the total number of particles given in Garrigues *et al.*[23], for the standard sparse PIC approach, $N_T = 5 \times 10^6$, and for the offset sparse PIC algorithm, $N_T = 1.1 \times 10^7$.

In Fig.9 we show the time and azimuthally averaged axial profiles of the electron properties (density and rms fluctuations, temperature) as well as the axial electric field profiles. The time averaging is done after convergence (physical time of 40 μs) to 4 μs with $M_t = 160$ equally spaced time shots. The rms axial profile of the electron density is calculated according to the following formula.

$$\delta n_{e,rms}(x) = \frac{1}{M_t}\sum_{k=1}^{M_t}\left[\frac{1}{M_y}\sum_{j=1}^{M_y} n_e^2(x,y_j,t_k) - \left(\frac{1}{M_y}\sum_{j=1}^{M_y} n_e(x,y_j,t_k)\right)^2\right]^{\frac{1}{2}} \quad (2)$$

where M_y is the number of nodes along the y direction, y_j corresponds to a given node position along the y direction, and t_k corresponds to a given time. In 2, the computations for the

PIC approach are performed with the standard bilinear projection, while the combination technique[23] at the coincident point of the regular grid is used for the series of sparse PIC computations.

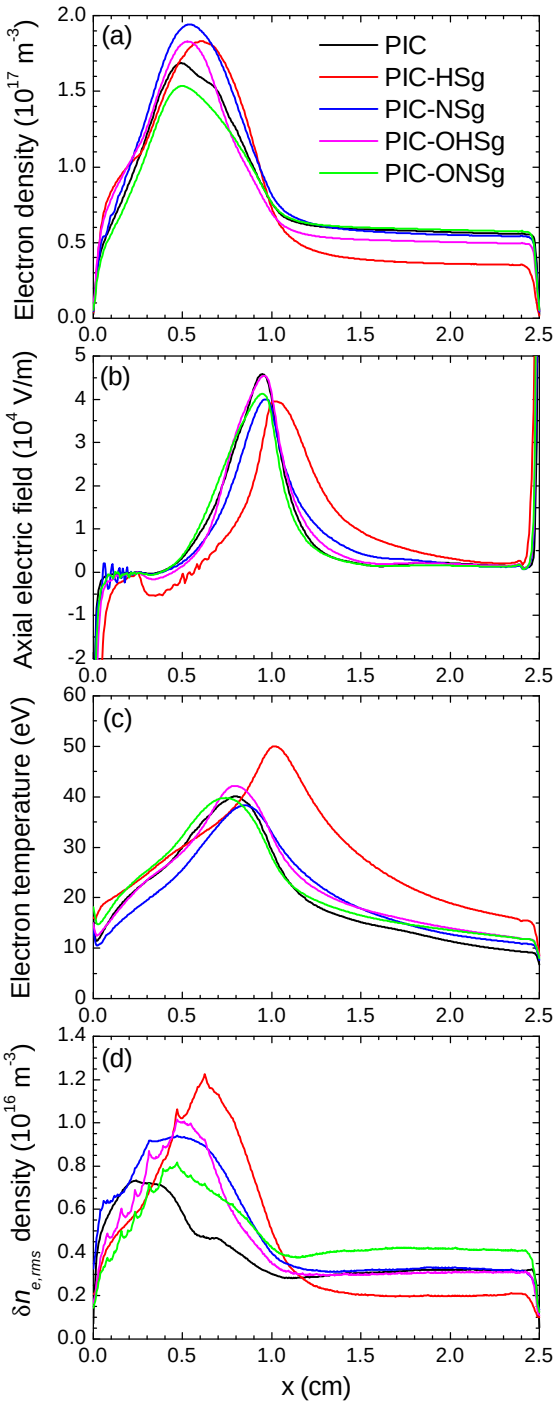

FIG. 9. Axial profiles of (a) electron density, (b) axial electric field, (c) electron temperature and (d) rms electron density fluctuations for the PIC and Sparse-PIC approaches (standard and offset methods for $l^0 = 3$ and $l^1 = 1$). The implementation of the two different methods to calculate the electric force acting on particles is also illustrated.

Taking the case with the regular PIC approach (indicated as PIC in Fig. 9), the standard sparse PIC algorithm with the hierarchical approach (PIC-HSg) shows a shift of the axial profiles of a few millimeters downstream of the peak of the solution obtained with the standard PIC algorithm, especially for the axial electric field and the electron temperature, which makes sense since the heating of the electron is controlled by the electric field. Very interestingly, the solution obtained with the nodal basis approach (PIC-NSg) is able to retrieve the profile of the plasma parameters with a good enough precision. This is due to the fact that the error associated with the recombination of the electric potential calculated on the regular grid nodes instead of the electric field calculated on the component grids directly at the particle location is reduced. The same conclusion was reached in the companion paper, but with much less effect[23]. Considering the calculations using the offset algorithms, the solutions become closer to the results of the standard PIC method. Even if the electron density is slightly underestimated, the use of the nodal sparse PIC algorithm (PIC-ONSg) again agrees better with the PIC results. Error calculations with the method presented in Ref.23 show an average error of 7 %, 32 %, 8 %, and 28 % for the electron density, rms fluctuations of the electron density, electron temperature, and axial electric field, respectively. Note that the same calculations for the electric field without the sheath regions show an error of about 10 %, in the same order of magnitude as the error calculations for the electron density and temperature. These error magnitudes are in the same range as the calculations without using the offset approach, but increasing n to 12, which corresponds to a regular grid of 4096^2 (see Ref. 22, but with the main drawback of almost no gain in computational speed). One way to assess the ability of the sparse method to properly recover the output of the standard PIC algorithm is to calculate the contribution of the injected current I_M from the source term to the ion beam current I_{ic} and the anode ion current I_{ia}, since $I_M = I_{ia} + I_{ic}$. We compare the results for the different methods in table IV. The I_{ia}/I_M and I_{ic}/I_M ratios are affected by the relative position of the source term (which is fixed) and the axial electric field profiles. The closest results to the standard PIC results are obtained with the nodal basis method and the best convergence for the PIC-ONSg algorithm.

The 2D profiles at a given time step are plotted in Fig. 10 for the PIC, PIC-HSg, PIC-NSg and PIC-ONSg methods for the same number of particles per cell. For the sparse PIC methods, the combination technique was used to calculate the ion density at the same grid nodes as the sparse PIC calculations. Comparing the 2D profiles of Fig.10a and b, the wavelength is different. From the spectrum integrated between x = 0.4 cm and x = 0.6 cm, the dominant mode measured by the Fast Fourier Transform is $k_y = 9\times10^3$ rad/m and $k_y = 5\times10^3$ rad/m, for the PIC and PIC-HSg, respectively. Also, the wave direction downstream of the magnetic field maximum seems to be in the $+y$ direction (opposite to the drift velocity as in Fig.10a). We have postulated in our previous work (see Garrigues *et al.*[22]) that the sparse approach acts as a kind of low-pass filter that is not able to fully recover the EDI instability observed in Hall thrusters with PIC simulations[17,19]. To

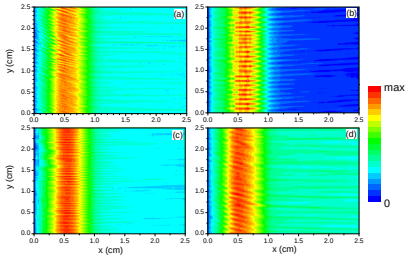

FIG. 10. 2D ion density profiles with the (a) PIC, (b) PIC-HSg,(c) PIC-NSg, and (d) PIC-ONSg algorithms. The maximum is 2×10^{17} m^{-3}, 2.2×10^{17} m^{-3}, 2.1×10^{17} m^{-3} and 1.7×10^{17} m^{-3}, respectively. Same conditions than Fig. 9.

reduce the grid-based error, the solution adopted was to increase the n level to 12, as already mentioned. In this way, the coarser resolution of the cells in the component grids is reduced and the spectrum of the instability tends to the one computed with the PIC model (with a dominant mode of k_y = 7.5×10^3 rad/m). The interesting conclusion of this study is that another factor can modify the solution of the problem and the signal of the spectrum. The quantity computed with the combination technique on the initial Cartesian grid for the electric potential or the electric field on the component grids has a strong effect on the results. This was not so obvious in our previous study[23]. This can be clearly seen by comparing the ion density profiles plotted in Figs. 10b and c with the PIC-HSg and PIC-NSg algorithms. The shape of the spectrum is different and the dominant mode changes from $k_y = 5\times10^3$ rad/m to $k_y = 10^4$ rad/m. Using the offset method tends to reduce the error. This is illustrated in Fig.10d with the PIC-ONSg algorithm. The shape of the ion density profile agrees with the PIC results of Fig.10a with the orientation of the EDI instability in the -y direction (with a dominant mode of k_y = 5.5×10^3 rad/m, which is slightly less than expected from the standard PIC simulations). It seems also that the choice in the quantity used for the combination technique is less critical when the offset method is used, the ion density profile with the PIC-OHSg algorithm is very similar to the one of the Fig.10d.

The saturation mechanism of the instability is related to ion wave trapping. It has been extensively documented in the literature[11,12,18]. One indication of such a mechanism is the broadening of the azimuthal ion velocity distribution function (IVDF) in the azimuthal direction. We show in Fig.11 the IVDF at two locations, one in the region of the appearance of the instability in the injection region and the other downstream where the instability is convected by the ions. The shape of the IVDF has already been analyzed in detail[11,12,18,22]. Here we want to highlight the effect of the sparse PIC algorithms on the ability to capture the IVDF. As expected, the error is largest with the PIC-HSg approach, the use of the offset sparse PIC algorithms is able to recover the tail of the IVDF with a population of ions corresponding to three orders less than the distribution peak.

We finish with the calculations of the acceleration factor, keeping the same number of particles per cell. The results are shown in the tableV. The gain obtained depends on the sparse PIC method used (standard or offset algorithms)

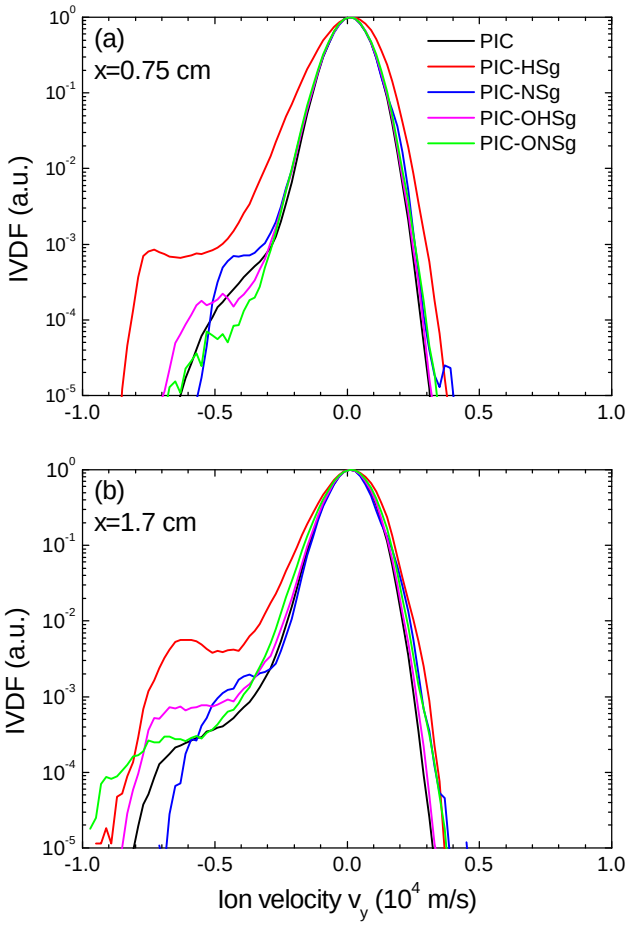

FIG. 11. Time-averaged azimuthal ion velocity distribution function at two axial different locations (a) $x = 0.75 \pm 0.1$ cm, and (b) $x = 1.7 \pm 0.1$ cm.

and the combination approaches (nodal or hierarchical). The higher speed-up factor is obtained with the PIC-HSg method, but the main drawback is the large error in the obtained solution. The most interesting result is that when comparing PIC-NSg and PIC-ONSg methods, the speed-up is almost identical. Of course, this cannot be generalized and is certainly related to the number of cores chosen. Nevertheless, it shows that the speed-up factor can be kept high by reducing the solution error. We need to understand this with a more refined

TABLE IV. I_{ia}/I_M and I_{ic}/I_M current ratio for the standard and sparse PIC algorithms

CASE	I_{ia}/I_M	I_{ic}/I_M
PIC	0.07	0.93
PIC-HSg	0.27	0.73
PIC-NSg	0.09	0.91
PIC-OHSg	0.16	0.84
PIC-ONSg	0.08	0.92

TABLE V. Speed up factor

CASE	factor
PIC-HSg	5.6
PIC-NSg	4.8
PIC-OHSg	3.2
PIC-ONSg	4.9

analysis.

IV. DISCUSSION

We want to emphasize that the calculations made for the cusp-type magnetic field benchmark are typically in the range of parameters encountered for most plasma source applications, but not for all. The typical Kaufman ion source used for gridded ion engines is below 100 G and pressures in the range of 1-10 mTorr[37]. In magnetron type discharges, especially for high power pulse configuration for sputtering, the rod of magnets are typically separated by a few centimeters, the pressure is still in the range of 1 to 10 mTorr, but the magnetic field strength can vary from 200 G[38] to more than 1500 G[39] depending on the applications. When magnetic field reaches higher value than in this study, the use of higher l^0 parameter is certainly the solution. For higher plasma region, and increase of n level is necessary (which is also the case for the regular PIC method to maintain the resolution of the electron Debye length). However, the very extensive studies of magnetron discharges (DC and HiPIMS regimes) have revealed the existence of a number of instabilities and structures at small scales/MHz wave range[40] and large scales/kHz wave range[39,41] that can also be coupled[40]. Dedicated PIC simulations have been carried out to investigate the origin of these instabilities[42,43]. The first step would be to reproduce these results with the sparse PIC algorithm. In a second time, the use of the sparse PIC approach would be interesting for example to study 3D effects.

In electron cyclotron resonance (ECR) discharge, together with the cusp magnetic field configuration, a microwave is injected to continuously heat the electrons in a zone called the resonance zone[44]. The condition for an efficient electron heating mechanism in the resonance zone is that the electron cyclotron pulsation $\omega_{ce} = eB/m_e$ (where e is the elementary charge) must be equal to the wave frequency ω. For a standard frequency of 2.45 GHz, the resonant magnetic field is 875 G, which remains in the order of magnitude typical of this study. However, to achieve very high plasma densities, for example for the production of highly charged ions in ECR ion sources[45], the frequency can be set as high as 10 GHz, and the resonant magnetic field can reach a very high magnitude ($\sim$ 3600 G). The self-consistent description of the coupling of the energy wave with the plasma also requires the resolution of Maxwell's equations (electromagnetic PIC scheme), which is beyond the scope of this study. The applicability of the sparse approach in combination with electromagnetic PIC algorithms must first be demonstrated before self-consistent simulations of ECR plasma sources can be addressed.

In the End-Hall source used for plasma processing, the operating pressure is of the order of 5 mTorr, the maximum of the magnetic field reaches 800 G (with a topology of magnetic field lines close to a magnetic field nozzle type expansion[46]). The order of magnitude of the plasma density is in the same range as that of the Hall thruster. Intuitively, we see no difficulty in using the sparse PIC approach with the offset method to capture the effect of strong anisotropy between parallel vs. perpendicular electron transport (as far as no occurrence of instabilities has been reported in the literature). Penning discharges can be operated at very low gas pressures down to 0.1 mTorr (and down to a few mTorr) with typical dimensions of a few centimeters. The magnetic field is nearly uniform with a strength of about 100 G[47,48] and a direction parallel to the chamber walls. Plasma densities are still below those of Hall thrusters. The main issue is the existence of spoke regimes (large scale and low frequency) responsible for the transport of charged particles through the magnetic field[47]. Plasma columns dedicated to the study of charged particle transport and whose configuration is similar to a Penning discharge, but the magnetic field strength can exceed that of a Penning discharge to magnetize the ions, also reveal the appearance of rotating structures[49,50]. One of our next steps is to challenge the sparse PIC approach to these types of magnetized plasmas before extending its application to very large plasma densities (and dimensions) such as the tokamak divertor plasma sheath edge.

V. CONCLUSIONS

We have compared the regular PIC and the sparse PIC algorithms (which are detailed in Ref.23) to check the accuracy of this later in the modeling of the partially magnetized low temperature plasmas. The analysis of the results shows that the use of the standard sparse PIC approach qualitatively agrees well with the regular PIC results, but with a large error. The combination method used to calculate the electric field at the location of the charged particles induces a large grid-based error. This is due to the error in capturing the anisotropic transport of electrons induced by the magnetic field when the mesh size of the component grids is too coarse. The use of

the offset sparse PIC algorithm, which consists in excluding the more anisotropic grids and reducing the coarser resolution of the mesh size, minimizes the grid-based error and the agreement with the results of the regular PIC algorithm is better. Another important result is that the grid-based error is not only influenced by the mesh size of the component grids, but also by the method used for the combination technique. After solving Poisson's equation on each of the component meshes, we tested two methods. In the first method, the combination technique is used to compute the electric potential at the regular grid nodes, differentiating the potential to compute the electric field, then a bi-linear weighting scheme is used to interpolate the electric field at the particle location (the algorithm is called the nodal algorithm in this study). In the second method, the electric field at the particle location is calculated directly from the combination of the electric fields calculated at the particle location in each of the component grids (this is the hierarchical algorithm). The results show that in the case of the Hall thruster EDI instability, the first algorithm reduces the grid-based error when the standard sparse PIC scheme is used, while the benefit is less pronounced for the offset sparse PIC method. The last important result is that the nodal algorithm tends to maintain a large speed-up factor with the offset sparse PIC method, which is not obvious since to keep the same statistic when the total number of cells increases, so does the total number of particles. This result needs further analysis.

The benchmark of the multi-cusp magnetic field discharge has shown the wide range of input parameters (pressure and magnetic field strength) where the sparse PIC algorithm with the offset method is able to reproduce the regular PIC calculations with less than 5 % of error. Very interestingly, the sparse PIC algorithm is able to recover the double-sheath layer formed in front of the dielectric walls at high magnetic field. When the pressure is less than 0.1 mTorr and the magnetic field is greater than 400 G, the solution is to increase the resolution by reducing the mesh size of the component grids by playing with the parameters of the offset sparse PIC method. Focusing on the Hall thruster benchmark and the EDI instability, the offset sparse PIC algorithm is again able to retrieve the plasma properties, including the ion velocity distribution functions and the ion population heated by the azimuthal instability. We have mentioned several test cases that we plan to work on. We are currently investigating the case of rotating spoke structures observed in Penning type discharges.

ACKNOWLEDGMENTS

M. Chung-To-Sang benefits from an Ecole Normale Supérieure - Paris Saclay PhD grant. C. Guillet benefits from a PhD grant of the Université de Toulouse Midi-Pyrénées-Région Occitanie. This work was granted access to the HPC resources of CALMIP supercomputing center under the allocation 2013-P1125. This work is funded by l'Agence Nationale de la Recherche (ANR) under the projet ANR-22-CE46-0012. Part of has been carried out within the framework of the EUROfusion Consortium, funded by the European Union via the Euratom Research and Training Programme (Grant Agreement No 101052200 — EUROfusion). Views and opinions expressed are however those of the author(s) only and do not necessarily reflect those of the European Union or the European Commission. Neither the European Union nor the European Commission can be held responsible for them.

AUTHOR DECLARATIONS

Conflict of interest

The authors have no conflicts to disclose

Author Contributions

L. Garrigues: Conceptualization (lead); Data curation (lead); Formal analysis (equal); Funding acquisition (equal); Investigation (equal); Methodology (equal); Project administration (lead); Resources (equal); Software (equal); Supervision (lead); Validation (lead); Visualization (lead); Writing – original draft (lead); Writing – review & editing (equal). **M. Chung-To-Sang:** Conceptualization (supporting); Formal analysis (equal); Investigation (equal); Methodology (equal); Resources (equal); Supervision (equal); Validation (equal); Visualization (supporting); Writing – review & editing (equal). **G. Fubiani:** Conceptualization (supporting); Data curation (supporting); Formal analysis (equal); Funding acquisition (equal); Investigation (equal); Methodology (equal); Project administration (equal); Resources (equal); Software (equal); Supervision (equal); Validation (equal); Visualization (supporting); Writing – review & editing (equal). **C. Guillet:** Formal analysis (equal); Investigation (equal); Methodology (equal); Supervision (equal); Validation (equal); Visualization (supporting); Writing – review & editing (equal). **F. Deluzet:** Formal analysis (equal); Funding acquisition (equal); Investigation (equal); Methodology (equal); Project administration (equal); Software (equal); Supervision (equal); Validation (equal); Visualization (supporting); Writing – review & editing (equal). **J. Narski:** Formal analysis (equal); Funding acquisition (equal); Investigation (equal); Methodology (equal); Project administration (equal); Software (equal); Supervision (equal); Validation (equal); Visualization (supporting); Writing – review & editing (equal).

DATA AVAILABILITY

The data that support the findings of this study are available from the corresponding author upon reasonable request.

REFERENCES

[1]R. Limpaecher and K. R. MacKenzie, "Magnetic Multipole Containment of Large Uniform Collisionless Quiescent Plasmas," Review of Scientific Instruments **44**, 726–731 (2003), https://pubs.aip.org/aip/rsi/article-pdf/44/6/726/8362682/726_1_online.pdf.

[2]M. Sadowski, "Spherical Multipole Magnets for Plasma Research," Review of Scientific Instruments **40**, 1545–1549 (1969), https://pubs.aip.org/aip/rsi/article-pdf/40/12/1545/8357540/1545_1_online.pdf.

[3]M. Yoshikawa, T. Ohkawa, and A. A. Schupp, "Plasma Confinement in a Toroidal Quadrupole," The Physics of Fluids **12**, 1926–1938 (1969), https://pubs.aip.org/aip/pfl/article-pdf/12/9/1926/12270711/1926_1_online.pdf.

[4]B. Wolf, R. Becker, T. Jolly, J. Ishikawa, P. Strehl, I. Brown, G. Alton, P. Spaedtke, H. Horneff, F. Bourg, *et al.*, *Handbook of Ion Sources* (CRC Press, 2020).

[5]Y. Jiang, G. Fubiani, L. Garrigues, and J. P. Boeuf, "Magnetic cusp confinement in low-beta plasmas revisited," Physics of Plasmas **27**, 113506 (2020), https://pubs.aip.org/aip/pop/article-pdf/doi/10.1063/5.0014058/16102487/113506_1_online.pdf.

[6]S. Mazouffre, "Electric propulsion for satellites and spacecraft: established technologies and novel approaches," Plasma Sources Science and Technology **25**, 033002 (2016).

[7]I. Levchenko, S. Xu, S. Mazouffre, D. Lev, D. Pedrini, D. Goebel, L. Garrigues, F. Taccogna, and K. Bazaka, "Perspectives, frontiers, and new horizons for plasma-based space electric propulsion," Physics of Plasmas **27**, 020601 (2020), https://pubs.aip.org/aip/pop/article-pdf/doi/10.1063/1.5109141/15770083/020601_1_online.pdf.

[8]D. M. Goebel, I. Katz, and I. G. Mikellides, "Conventional Hall thrusters," in *Fundamentals of Electric Propulsion, 2nd Edition* (John Wiley & Sons, Ltd, 2023) Chap. 7, pp. 269–336.

[9]S. P. Gary, "Electrostatic component/component instabilities in uniform plasmas," in *Theory of Space Plasma Microinstabilities*, Cambridge Atmospheric and Space Science Series (Cambridge University Press, 1993) p. 30–66.

[10]A. Ducrocq, J. C. Adam, A. Héron, and G. Laval, "High-frequency electron drift instability in the cross-field configuration of Hall thrusters," Physics of Plasmas **13**, 102111 (2006), https://pubs.aip.org/aip/pop/article-pdf/doi/10.1063/1.2359718/15622711/102111_1_online.pdf.

[11]T. Lafleur, S. D. Baalrud, and P. Chabert, "Theory for the anomalous electron transport in Hall effect thrusters. II. Kinetic model," Physics of Plasmas **23**, 053503 (2016), https://pubs.aip.org/aip/pop/article-pdf/doi/10.1063/1.4948496/15938778/053503_1_online.pdf.

[12]T. Lafleur, S. D. Baalrud, and P. Chabert, "Characteristics and transport effects of the electron drift instability in Hall-effect thrusters," Plasma Sources Science and Technology **26**, 024008 (2017).

[13]F. Petronio, T. Charoy, A. Alvarez Laguna, A. Bourdon, and P. Chabert, "Two-dimensional effects on electrostatic instabilities in Hall thrusters. II. Comparison of particle-in-cell simulation results with linear theory dispersion relations," Physics of Plasmas **30**, 012104 (2023), https://pubs.aip.org/aip/pop/article-pdf/doi/10.1063/5.0119255/16660850/012104_1_online.pdf.

[14]S. Tsikata, N. Lemoine, V. Pisarev, and D. M. Grésillon, "Dispersion relations of electron density fluctuations in a Hall thruster plasma, observed by collective light scattering," Physics of Plasmas **16**, 033506 (2009), https://pubs.aip.org/aip/pop/article-pdf/doi/10.1063/1.3093261/14079331/033506_1_online.pdf.

[15]J. Cavalier, N. Lemoine, G. Bonhomme, S. Tsikata, C. Honoré, and D. Grésillon, "Hall thruster plasma fluctuations identified as the E×B electron drift instability: Modeling and fitting on experimental data," Physics of Plasmas **20**, 082107 (2013), https://pubs.aip.org/aip/pop/article-pdf/doi/10.1063/1.4817743/16744431/082107_1_online.pdf.

[16]S. Tsikata, J. Cavalier, A. Héron, C. Honoré, N. Lemoine, D. Grésillon, and D. Coulette, "An axially propagating two-stream instability in the Hall thruster plasma," Physics of Plasmas **21**, 072116 (2014), https://pubs.aip.org/aip/pop/article-pdf/doi/10.1063/1.4890025/15690993/072116_1_online.pdf.

[17]J. P. Boeuf and L. Garrigues, "E × B electron drift instability in Hall thrusters: Particle-in-cell simulations vs. theory," Physics of Plasmas **25**, 061204 (2018), https://doi.org/10.1063/1.5017033.

[18]T. Lafleur and P. Chabert, "The role of instability-enhanced friction on 'anomalous' electron and ion transport in Hall-effect thrusters," Plasma Sources Science and Technology **27**, 015003 (2017).

[19]T. Charoy, J. P. Boeuf, A. Bourdon, J. A. Carlsson, P. Chabert, B. Cuenot, D. Eremin, L. Garrigues, K. Hara, I. D. Kaganovich, A. T. Powis, A. Smolyakov, D. Sydorenko, A. Tavant, O. Vermorel, and W. Villafana, "2D axial-azimuthal particle-in-cell benchmark for low-temperature partially magnetized plasmas," Plasma Sources Science and Technology **28**, 105010 (2019).

[20]K. Hara and S. Tsikata, "Cross-field electron diffusion due to the coupling of drift-driven microinstabilities," Physical Review E **102**, 023202 (2020).

[21]P. Kumar, S. Tsikata, and K. Hara, "Effects of multiply charged ions on microturbulence-driven electron transport in partially magnetized plasmas," Journal of Applied Physics **130**, 173307 (2021), https://pubs.aip.org/aip/jap/article-pdf/doi/10.1063/5.0067305/15271804/173307_1_online.pdf.

[22]L. Garrigues, B. Tezenas du Montcel, G. Fubiani, and B. C. G. Reman, "Application of sparse grid combination techniques to low temperature plasmas Particle-In-Cell simulations. II. electron drift instability in a hall thruster," Journal of Applied Physics **129**, 153304 (2021), https://doi.org/10.1063/5.0044865.

[23]L. Garrigues, M. Chung-To-Sang, G. Fubiani, C. Guillet, F. Deluzet, and J. Narski, "Acceleration of Particle-In-Cell using Sparse Grid Algorithms. I. Application to Low Temperature Plasmas," (article submitted in) Physics of Plasmas (2024).

[24]M. A. Lieberman and A. J. Lichtenberg, "Diffusion and transport," in *Principles of Plasma Discharges and Materials Processing* (John Wiley & Sons, Ltd, 2005) Chap. 5, pp. 133–163, https://onlinelibrary.wiley.com/doi/pdf/10.1002/0471724254.ch5.

[25]D. Leitner and C. Lyneis, "ECR ion sources," in *The Physics and Technology of Ion Sources* (John Wiley & Sons, Ltd, 2004) Chap. 11, pp. 203–231, https://onlinelibrary.wiley.com/doi/pdf/10.1002/3527603956.ch11.

[26]A. J. Marcus, G. Knorr, and G. Joyce, "Two-dimensional simulation of cusp confinement of a plasma," Plasma Physics **22**, 1015 (1980).

[27]L. Garrigues, G. Fubiani, and J. P. Boeuf, "Appropriate use of the Particle-In-Cell method in low temperature plasmas: Application to the simulation of negative ion extraction," Journal of Applied Physics **120**, 213303 (2016), https://pubs.aip.org/aip/jap/article-pdf/doi/10.1063/1.4971265/13442817/213303_1_online.pdf.

[28]L. Garrigues and G. Fubiani, "Tutorial: Modeling of the extraction and acceleration of negative ions from plasma sources using particle-based methods," Journal of Applied Physics **133**, 041102 (2023), https://doi.org/10.1063/5.0128759.

[29]G. Fubiani, L. Garrigues, G. Hagelaar, N. Kohen, and J. P. Boeuf, "Modeling of plasma transport and negative ion extraction in a magnetized radio-frequency plasma source," New Journal of Physics **19**, 015002 (2017).

[30]"LXCat, Plasma Data Exchange Project," `https://lxcat.net`, Phelps database, updated, 6 June 2011.

[31]A. V. Phelps, "The application of scattering cross sections to ion flux models in discharge sheaths," Journal of Applied Physics **76**, 747–753 (1994), https://doi.org/10.1063/1.357820.

[32]L. F. Ricketson and A. J. Cerfon, "Sparse grid techniques for particle-in-cell schemes," Plasma Physics and Controlled Fusion **59**, 024002 (2016).

[33]S. Muralikrishnan, A. J. Cerfon, M. Frey, L. F. Ricketson, and A. Adelmann, "Sparse grid-based adaptive noise reduction strategy for particle-in-cell schemes," Journal of Computational Physics: X **11**, 100094 (2021).

[34]F. Deluzet, G. Fubiani, L. Garrigues, C. Guillet, and J. Narski, "Efficient parallelization for 3D-3V sparse grid Particle-in-Cell: shared memory systems architectures," Journal of Computational Physics **480**, 112022 (2023).

[35]J. A. Bittencourt, "Charged particle motion in nonuniform magnetostatic fields," in *Fundamentals of Plasma Physics* (Springer New York, 2004) pp. 59–94.

[36]L. Garrigues, B. Tezenas du Montcel, G. Fubiani, F. Bertomeu, F. Deluzet, and J. Narski, "Application of sparse grid combination techniques to low temperature plasmas Particle-In-Cell simulations. I. Capacitively coupled radio frequency discharges," Journal of Applied Physics **129**, 153303 (2021), https://doi.org/10.1063/5.0044363.

[37]D. M. Goebel, I. Katz, and I. G. Mikellides, "Ion thruster plasma generators," in *Fundamentals of Electric Propulsion, 2nd Edition* (John Wiley & Sons, Ltd, 2023) Chap. 5, pp. 155–228.

[38]J. W. Bradley, A. Mishra, and P. J. Kelly, "The effect of changing the magnetic field strength on hipims deposition rates," Journal of Physics D: Applied Physics **48**, 215202 (2015).

[39]A. Anders, P. Ni, and A. Rauch, "Drifting localization of ionization runaway: Unraveling the nature of anomalous transport in high power impulse magnetron sputtering," Journal of Applied Physics **111**, 053304 (2012), https://pubs.aip.org/aip/jap/article-pdf/doi/10.1063/1.3692978/16709250/053304_1_online.pdf.

[40]S. Tsikata and T. Minea, "Modulated electron cyclotron drift instability in a high-power pulsed magnetron discharge," Physical Review Letters **114**, 185001 (2015).

[41]A. Hecimovic, C. Corbella, C. Maszl, W. Breilmann, and A. von Keudell, "Investigation of plasma spokes in reactive high power impulse magnetron sputtering discharge," Journal of Applied Physics **121**, 171915 (2017), https://pubs.aip.org/aip/jap/article-pdf/doi/10.1063/1.4978348/15194367/171915_1_online.pdf.

[42]A. Revel, T. Minea, and C. Costin, "2D PIC-MCC simulations of magnetron plasma in hipims regime with external circuit," Plasma Sources Science and Technology **27**, 105009 (2018).

[43]J. P. Boeuf, "Spoke formation in low temperature E×B plasmas: Transition from gradient-drift instability to ionization wave," Physics of Plasmas **30**, 022112 (2023), https://pubs.aip.org/aip/pop/article-pdf/doi/10.1063/5.0136888/16682177/022112_1_online.pdf.

[44]M. A. Lieberman and A. J. Lichtenberg, "Wave-heated discharges," in *Principles of Plasma Discharges and Materials Processing* (John Wiley & Sons, Ltd, 2005) Chap. 13, pp. 491–534, https://onlinelibrary.wiley.com/doi/pdf/10.1002/0471724254.ch13.

[45]R. Geller, *Electron Cyclotron Resonance Ion Source and ECR plasmas* (Taylor and Francis, New York, 1996).

[46]N. Oudini, G. J. M. Hagelaar, J.-P. Boeuf, and L. Garrigues, "Physics and modeling of an end-Hall (gridless) ion source," Journal of Applied Physics **109**, 073310 (2011), https://pubs.aip.org/aip/jap/article-pdf/doi/10.1063/1.3572053/15068188/073310_1_online.pdf.

[47]A. T. Powis, J. A. Carlsson, I. D. Kaganovich, Y. Raitses, and A. Smolyakov, "Scaling of spoke rotation frequency within a Penning discharge," Physics of Plasmas **25**, 072110 (2018), https://pubs.aip.org/aip/pop/article-pdf/doi/10.1063/1.5038733/14759753/072110_1_online.pdf.

[48]J. Y. Kim, J. Choi, J. Choi, Y. S. Hwang, and K.-J. Chung, "Efficiency improvement of an $\boldsymbol{E} \times \boldsymbol{B}$ penning discharge source by enhanced cross-field transport of electrons," Plasma Sources Science and Technology **31**, 05LT02 (2022).

[49]V. Gonzalez-Fernandez, P. David, R. Baude, A. Escarguel, and Y. Camenen, "Spatially resolved determination of the electronic density and temperature by a visible spectro-tomography diagnostic in a linear magnetized plasma," Scientif Reports **10**, 5389 (2020).

[50]S. Vincent, V. Dolique, and N. Plihon, "High-speed imaging of magnetized plasmas: When electron temperature matters," Physics of Plasmas **29**, 032104 (2022), https://pubs.aip.org/aip/pop/article-pdf/doi/10.1063/5.0083130/16646793/032104_1_online.pdf.